The Effect of Turbulence Modeling on the Mixing Characteristics of Several Fuel Injectors at Hypervelocity Flow Conditions.

Tomasz G. Drozda,* Jacob J. Lampenfield,† Rohan G. Deshmukh,‡Robert A. Baurle,§
and
J. Philip Drummond,¶
NASA Langley Research Center, Hampton, VA, 23681

CFD analysis is presented on the effects of turbulence modeling choices on the mixing characteristics and performance of three fuel injectors at hypervelocity flow conditions. The analyses were carried out with the VULCAN-CFD solver using Reynolds-Averaged Simulations (RAS). The hypervelocity flow conditions match the high Mach number flow of the experiments conducted as a part of the Enhanced Injection and Mixing Project (EIMP) at the NASA Langley Research Center. The three injectors are the baseline configurations used in the experiments and represent three categories of injectors typically considered individually or in combination for fueling high-speed propulsive devices. The current work discusses the impact of the turbulence model and the turbulent Schmidt number on the mixing flow field behavior and the mixing performance as described by the one-dimensional values of the Mach number, total pressure recovery, and the mixing efficiency. Because planar laser induced fluorescence (PLIF) images are available from the EIMP experiments, the sensitivity of the synthetic LIF signal to turbulence modeling choices is also examined to determine whether PLIF can be extended beyond its intended qualitative visualization purpose and used to guide CFD turbulence model and parameter selections. It is found that the mixing performance, as quantified using mixing efficiency, exhibits a strong sensitivity to both turbulence model choice and turbulent Schmidt number value. However, the synthetic LIF signal only demonstrates a modest level of sensitivity, which suggests that PLIF is of limited use for guiding CFD turbulence model and parameter selections.

I. Introduction

FUEL injector design, leading to efficient fuel-air mixing, combustion, and flameholding, remains one of the key challenges in scramjet flowpath design. Attempts to improve the fuel-air mixing, while simultaneously reducing total pressure losses, have received a great deal of attention over the years.[1] Although some total pressure loss is thermodynamically unavoidable and occurs as a result of the desired effect of molecular mixing of the fuel and air, any losses, beyond this minimum amount reduce the thrust potential of the engine and should be minimized.

The Enhanced Injection and Mixing Project (EIMP), being executed at the NASA Langley Research Center, represents an effort to achieve more rapid mixing at high speeds.[2] The EIMP aims to investigate scramjet fuel injection and mixing physics, improve the understanding of underlying physical processes, and develop enhancement strategies relevant to flight Mach numbers greater than eight. In the experiments, which are underway in the Arc-Heated Scramjet Test Facility (AHSTF), various fuel injection devices are being tested on an open flat plate located downstream of a Mach 6 facility nozzle, which emulates the combustor of a flight vehicle traveling at a Mach number of about 14 to 16. An open flat plate geometry was chosen, as opposed to a duct, in order to facilitate optical access for nonintrusive diagnostics and to simplify the experiment. The experiments utilize the nitric oxide (NO) planar (P) laser-induced

*Research Aerospace Engineer, Hypersonic Airbreathing Propulsion Branch, AIAA Associate Fellow.
†Research Engineer, Analytical Mechanics Associates, Inc., AIAA Member.
‡Graduate Research Assistant, Space Flight Projects Laboratory, Purdue University, West Lafayette, IN, 47907
§Research Aerospace Engineer, Hypersonic Airbreathing Propulsion Branch, AIAA Associate Fellow.
¶NASA Distinguished Research Associate, AIAA Fellow.

fluorescence (LIF), or NO PLIF, for flow visualization. The NO-PLIF takes advantage of the NO that naturally exists in low concentration in the facility air[3] as a result of the electric-arc heating process. This facility-air-NO acts as an in situ flow tracer that can be imaged using PLIF. Furthermore, the tests are conducted at a reduced total temperature to allow for uncooled test hardware and use helium in order to focus on mixing and reduce the complexity and cost of the experiment. The mixing characteristics of three baseline fuel injectors: strut, ramp and flushwall, under the experimental conditions, have been previously obtained computationally.[4,5] The results of the numerical simulations were also used, along with a LIF model for NO, to produce a synthetic LIF signal, which is used to obtain computational flow images (CFI) for direct comparisons with those obtained experimentally using NO PLIF technique.[6–8] The CFIs were previously used to successfully identify several "global" issues with the RAS simulations, such as incorrect wall temperature boundary conditions and early onset of turbulent flow transition, as discussed by Drozda et al.[7] Since no quantitative experimental data were available in the previous studies, Reynolds Averaged Simulations (RAS) were utilized with the turbulence model and turbulent Schmidt number ($\mathrm{Sc_t}$) selected based on subject-matter-expert experience with similar flows. In the present study, computational simulations are utilized with the goal of assessing the impact that the turbulence models and $\mathrm{Sc_t}$ have on the mixing flowfield. The mixing parameters of interest, including one-dimensional Mach number, total pressure recovery, and mixing efficiency, are computed and compared for various cases, including for a range of fuel equivalence ratios (ERs). Furthermore, a numerical assessment is made of the sensitivity of the LIF to the turbulence model and $\mathrm{Sc_t}$. This is accomplished by visually comparing CFIs obtained from RAS using various turbulence models and $\mathrm{Sc_t}$ to each other and available experimental PLIF data. The goal of this aspect of the work is to evaluate the possibility of selecting either turbulence model and/or $\mathrm{Sc_t}$ for the RAS using experimentally-obtained PLIF visualization data.

II. Injector Geometries and Simulated Flow Conditions

Three types of injectors are investigated in the current study. These are a strut, ramp, and rectangular, high-aspect ratio flushwall injector. The strut and a ramp have been previously studied by Baurle et al.[9] at a combustor entrance Mach number of 4.5. However, unlike the simulations of Baurle et al.[9] that configured the injectors on opposite walls of a closed duct and in an interdigitated fashion, the current simulations include a row of injectors on an open flat plate. The flat plate is 28.87 inches long tip-to-tail with the fuel injection plane located at 8.87 inches downstream from the leading edge of the plate. The flushwall injector geometry is based on the multiobjective optimization work of Ogawa.[10] Isometric views and dimensional details of the strut, ramp, and flushwall injectors are shown in Figs. 1-3, where x, y, and z denote the streamwise (or downstream), vertical (or wall normal), and cross-stream directions, respectively.

The struts, shown in Fig. 1, are placed 0.9 inches apart in the z-direction. This spacing is the same as that found in the previous work of Baurle et al.[9] Each strut injector has four fuel ports. The lower three ports are aligned with the x-axis, while the the top-most port is rotated counterclockwise by 20 degrees in the xy-plane. Each injector port has a throat diameter of 0.083 inches followed by a conical expansion area with a half-angle of 6 degrees (not shown) that expands helium "fuel" to an exit Mach number of approximately 3.0.

The ramp injectors, shown in Fig. 2, are spaced 1.2 inches apart in the z-direction. This spacing is also the same as that found between the interdigitated ramp configuration of Baurle et al.[9] The ramp injector also has four fuel ports. The lower pair of ports is aligned with the x-axis, while the upper pair is rotated counterclockwise by 11.8 degrees in the xy-plane, and then outward by 10 degrees. Each injector port has a throat diameter of 0.108 inches followed by a conical expansion area with a half-angle of 10 degrees (not shown) that has the same expansion area ratio as the strut and expands helium to an exit Mach number of about 3.0.

The flushwall injectors, shown in Fig. 3, are spaced 0.852 inches apart in the the z-direction. The injector port has a rectangular cross-section with an aspect ratio of 8 at the injector exit plane, with the longer dimension aligned with the streamwise direction. The flushwall injector also contains an expansion section with a 6 degree half-angle (not shown). The injector exit expansion area ratio matches that of the conical fuel ports of both the strut and the ramp. The exit area also matches the total exit area of the 4 fuel ports of the strut. Unlike the strut and ramp, the flushwall injector does not introduce a physical blockage into the flow. However, a number of flow features form around the injection site that interact to produce a similar effect.

The freestream conditions of the flow approaching the fuel injectors correspond to a total pressure and total temperature of 4.31 MPa and 978 K, respectively, expanded to a Mach number of about 6.36. A thermally perfect mixture of 21% oxygen (O_2), 78% nitrogen (N_2), and 1% nitric oxide (NO) by volume was used for the air. A small amount of NO was present to account for production of this species in the experimental facility,[3] although its impact on the

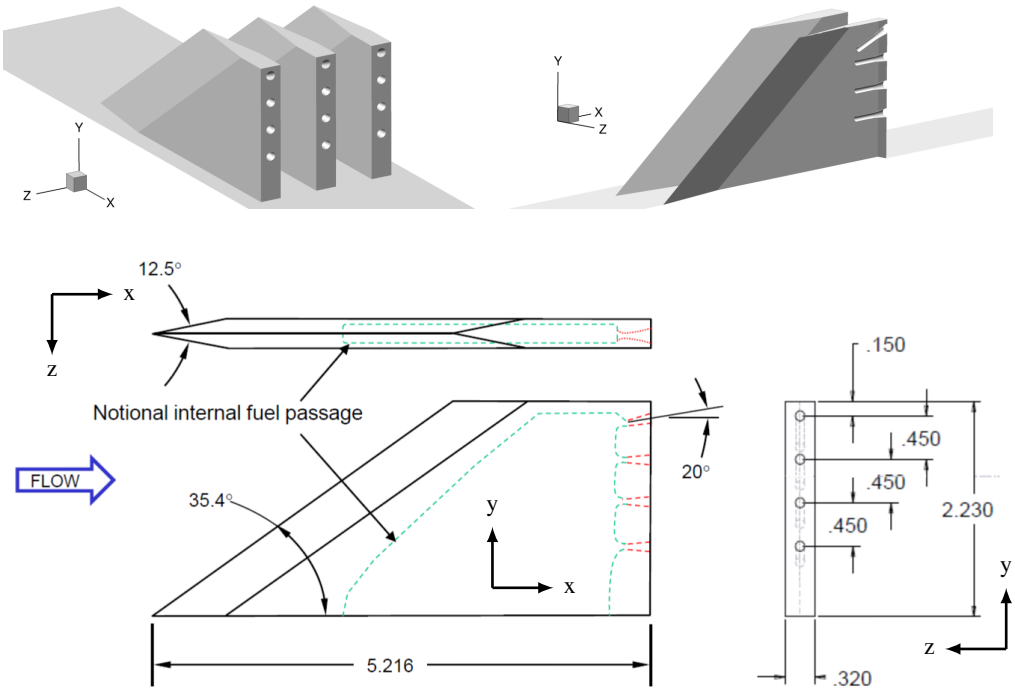

Figure 1. Isometric views and dimensional details of the baseline strut injector (dimensions are in inches).

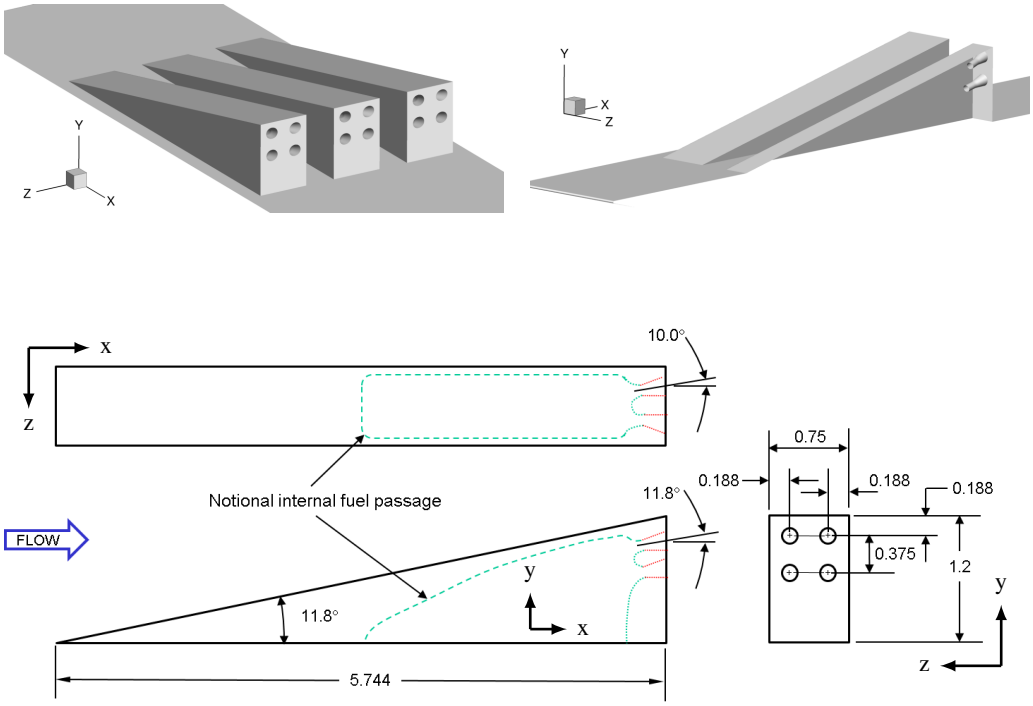

Figure 2. Isometric views and dimensional details of the baseline ramp injector (dimensions are in inches).

current simulations is expected to be negligible. The mass flow rate of helium for each injector was set equal to that computed for hydrogen assuming an ER of 0.75 over the intended fueling area (IFA). An IFA is established indepen-

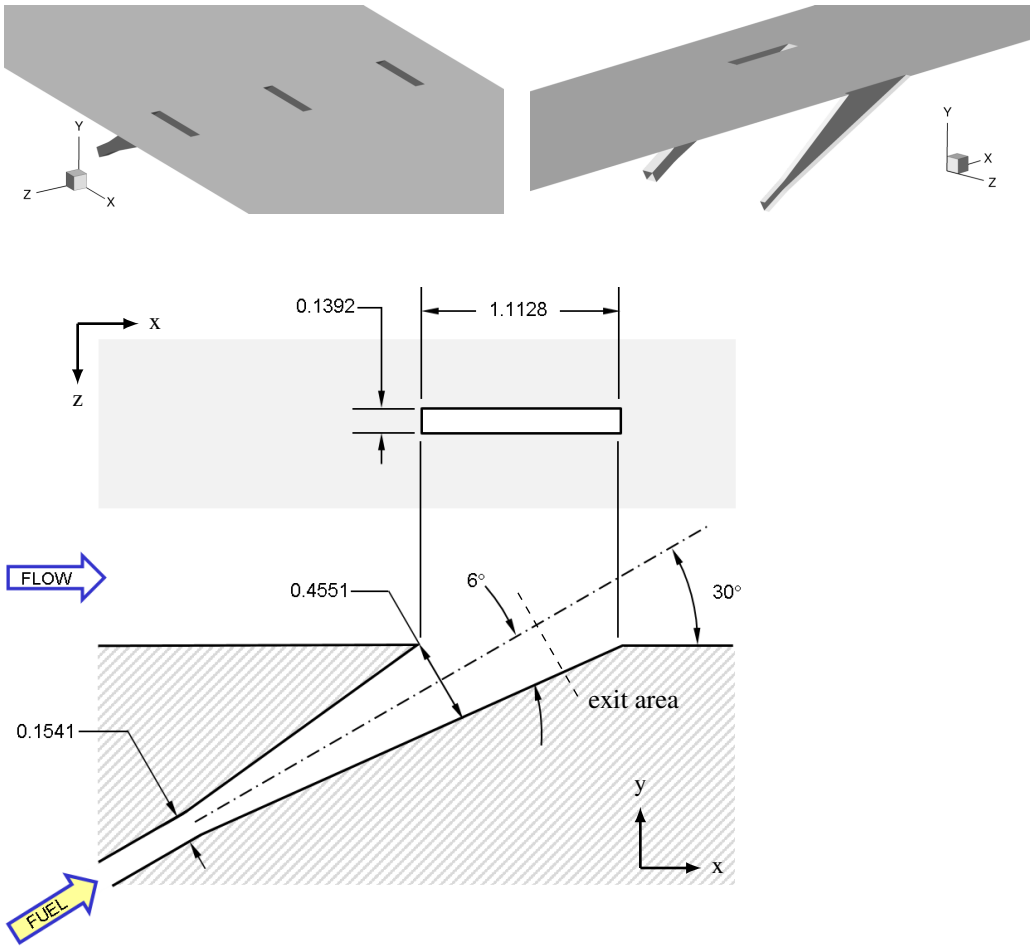

Figure 3. Isometric views and dimensional details of the baseline flushwall injector (dimensions are in inches).

dently for each injector based on a portion of the notional combustor cross-section area that each injector is designed to fuel. For example, a combustor cross-section area fueled with slender struts will likely require such devices to be spaced more closely than a similar combustor fueled with large vortex generating ramps. Therefore, the IFA will be narrower for struts than for the ramps. The IFAs for the strut and ramp are obtained from Baurle et al.[9] who investigated them in a realistic scramjet combustor configuration. Since the flushwall injector was designed with the intent to fuel the same flowpath, the IFA height for the flushwall injector is the same as that for the ramp with the width obtained from the optimization work of Ogawa.[10] Values of relevant global flow parameters for both fuel and air are provided in Table 1 for an ER of 0.75. The subscripts 0, f, and a denote *total* conditions, fuel, and air flow streams, respectively. All values are computed based on the flowpath entrance flow conditions for the air and the expanded flow conditions at the exit of the injector ports for the fuel. It should be noted that these values correspond to the nominal conditions used in, or obtained from, the CFD simulations. In addition to the quantities needed for the simulations, quantities that have been found to be important to injection and mixing in canonical problems[11–13] are also shown. These quantities are: the unit Reynolds number, Re'; the velocity difference parameter, ΔU; the convective Mach number, M_c; and the ratios of the fuel-to-air static density, $\rho_f \,/\, \rho_a$, static pressure, $p_f \,/\, p_a$, and dynamic pressure, $J_q = (\rho_f u_f^2)/(\rho_a u_a^2)$. Note that the two parameters that have leading order impact on small scale mixing, i.e., the velocity difference parameter and the convective Mach number, are the same for all cases, allowing the focus of the present study to be on the impact of turbulence modeling choices on the large-scale inviscid flow features and mixing.

Table 1. Nominal global parameters of interest for the strut, ramp, and flushwall injector configurations. The last five rows contain several nondimensional ratios of interest in mixing flows.

	Air†	Fuel Simulant (Helium)		
Property		Strut	Ramp	Flushwall
IFA ‡ W×H (in^2)		0.9 × 3.0	2.4 × 1.5	1.704 × 1.5
Mach	6.36	2.98	2.96	2.98
$P0$ (MPa)	4.309	0.224	0.0882	0.424
$T0$ (K)	977.8	293.15	293.15	293.15
P (kPa)	1.808	7.205	2.911	13.642
T (K)	112.4	74.14	74.91	74.14
u (m/s)	1353.6	1508.2	1505.6	1508.2
Re' (1/in) x10e3	259.4	358.4	286.2	339.3
$\dot{m}_a$ (kg/s) ×10e-3		131.68	175.57	124.65
$\dot{m}_f$ (kg/s) ×10e-3		2.884	3.845	2.730
ER§		0.75	0.75	0.75
ΔU¶		0.054	0.054	0.054
M_c‖		0.22	0.21	0.22
ρ_f / ρ_a		0.84	0.66	0.79
p_f / p_a		3.98	3.22	3.77
J_q**		1.04	0.83	0.99

†21% O_2, 78% N_2, 1% NO by volume
‡Intended fueling area for the injector expressed as width times height (W×H)
§ER with respect to the IFA
¶Velocity difference parameter, $\Delta U = (u_f - u_a)/(u_f + u_a)$
‖Convective Mach number, $M_c = |u_f - u_a|/(c_f + c_a)$, c denotes the speed of sound.
**Dynamic pressure ratio, $J_q = (\rho_f u_f^2)/(\rho_a u_a^2)$.

III. Metrics of Interest

A number of different metrics for mixing efficiency, thermodynamic losses, and thrust performance exist with a rigorous analysis proposed by Riggins et al.[14] For the current study, the following one-dimensional metrics were chosen: mass-flux-weighted Mach number, M_{1D}; the total pressure recovery, P_0^{rec}; and mixing efficiency, η_m, based on stoichiometric proportions of fuel and air. The mass-flux-weighted Mach number is obtained from:

$$M_{1D} = \frac{\int M \rho u \, dA}{\int \rho u \, dA}, \tag{1}$$

where M is the Mach number, the subscript 1D denotes a one-dimensional property, ρ is the static density, u and dA are the streamwise velocity component and the incremental area projected in the streamwise direction, respectively, and the integration is over a single cross-stream plane (yz-plane) of interest. This mass-flux-weighted Mach number is useful in revealing the global behavior of the flow and the extent of margin with respect to choked flow conditions. The mass-flux-weighted total pressure recovery is defined as:

$$P_o^{rec} = \frac{1}{P_{o_i}} \frac{\int P_o \rho u \, dA}{\int \rho u \, dA}, \tag{2}$$

where P_o, and P_{o_i} are the local and reference (e.g., free stream, flowpath entrance) values of the total pressure, respectively. This parameter is proportional to the difference between sensible entropies computed at the total and static values of the temperature and therefore gives a measure of the thermodynamic losses. For mixing simulations, the total pressure recovery quantifies the losses due to the drag on the injector bodies and the surface of the flat plate, the mechanical stirring induced by injector bodies (especially the ramp), the turbulence, and the molecular mixing. For reacting simulations, the total pressure recovery is further reduced by the entropy increases due to the chemical reactions (via heat addition and reactants-to-products conversion); therefore, the values of the total pressure recovery obtained from the mixing-only simulations can be thought of as the maximum achievable for a given injector. The

mixing efficiency is defined in this work following Mao et al.:[15]

$$\eta_m = \frac{\int Y_R \rho u \, dA}{\int Y \rho u \, dA} \tag{3}$$

where Y is the fuel or oxidizer mass fraction depending on whether the global ER is less than or greater than 1, respectively. The quantity Y_R is defined as the amount of fuel or oxidizer that would react if complete reaction took place without further mixing, i.e.,

$$Y_R = \begin{cases} Y, & Y \leq Y_{st} \\ \frac{Y_{st}}{1-Y_{st}}(1-Y), & Y > Y_{st} \end{cases} \tag{4}$$

where Y_{st} is the stoichiometric value of fuel or oxidizer mass fraction. For cases with overall ER of one, either fuel or oxidizer can be used in place of Y. However, choosing the fuel has a minor benefit of clarifying the meaning of Eq. (4), which becomes

$$Y_R = \begin{cases} Y_f, & Y_f \leq Y_{f,st} \\ FAR_{st}\, Y_a, & Y_f > Y_{f,st} \end{cases} \tag{5}$$

where subscripts f and a denote fuel and air streams, respectively. The quantity FAR_{st} denotes the stoichiometric value of the fuel-to-air ratio and equals to 0.0293 for hydrogen-air mixtures. It is clear from the above equation that if the local value of the mass fraction of fuel is less than its stoichiometric value, then that amount is "counted" as fully mixed because there is a sufficient amount of air to potentially deplete all of the fuel if reactions were allowed. However, when the local value of the fuel mass fraction is greater than its stoichiometric value, then the only part that could react is that which is in stoichiometric proportion to the local value of the mass fraction of the air. Therefore, only that portion is counted as being mixed in Eq. (3). The stoichiometric value of the hydrogen mass fraction is 0.0285. The mixing efficiency formula in Eq. (3) can also be used to analyze mixing in reacting simulations, however, since fuel and oxidizer are consumed to make combustion products, care must be taken to use the elemental mass fractions of either fuel or oxidizer (i.e., mass fractions of all elements that originate in either fuel or oxidizer streams).

IV. NO PLIF Modeling

In order to compare the simulation results to the experimentally obtained NO-PLIF flow visualizations, the LIF signal must be modeled and computed from the CFD. The LIF signal level, S (number of counts recorded on a pixel of the detector), is a function of temperature, pressure, mole-fraction, flow velocity, and a number of known experimental parameters. A model for the fluorescence signal in the weak fluorescence regime is given by Paul et al.:[16]

$$S \propto \frac{\chi_{NO}}{k_B T}\, \phi(P, T, \chi_\alpha) \sum_i \left(f_B(T, J)\, B_{12}(J)\, g(v_0, v_l, \Delta v_l, P, T, \chi_\alpha, u_\parallel) \right)_i , \tag{6}$$

where χ_{NO}, χ_α, P, T, k_B, f_B, J, B_{12}, g, v_0, v_l, Δv_l, and $u_\parallel$ are the mole fraction of NO and species α in the mixture, mixture pressure and temperature, Boltzmann constant, Boltzmann fraction, rotational quantum number, Einstein absorption coefficient, spectral overlap integral, transition line center absorption wavenumber, laser center wavenumber and full width at half maximum (FWHM), and velocity parallel to the laser sheet, respectively. The fluorescence yield, ϕ, is defined as

$$\phi = \frac{A_{21}}{A_{21} + Q(P, T, \chi_\alpha)}, \tag{7}$$

where A_{21} and Q are the Einstein spontaneous emission rate and quenching rate, respectively. The summation in Eq. 6 is over all transition lines i that are excited by the laser. The proportionality in Eq. 6 can be replaced with an equality by introducing a constant that describes the optical system. In addition, Eq. 6 contains nonlinear dependencies on pressure, temperature, and mole fraction of species in the mixture through the Boltzmann fraction, the spectral overlap integral, and the quenching rate. Furthermore, the spectral overlap integral also accounts for signal attenuation due to laser "detuning" from the intended transition line, and the Doppler effect. All quantities are modeled following the assumptions and the approach of Paul et al.[16] and Ivey et al.[17] with the model constants and coefficients obtained from LIFBASE.[18] The detailed analysis of the applicability and accuracy of the above model for current application was discussed by Drozda et al.[8]

The above model was applied to the CFD data to obtain CFIs equivalent to those obtained experimentally with PLIF. However, it should be noted that, due to the strong nonlinearities in the model, applying it to the RAS data, which represents time-averages, is expected to introduce some errors. This is in contrast to the experimentally obtained PLIF images, which are instantaneous by nature and time-averaged in the post-processing step. Consequently, the LIF signal obtained from RAS (i.e., CFI) is only an approximation of the experimental PLIF, i.e.,

$$S_{RAS}(\overline{P}, \overline{T}, \overline{\chi_\alpha}, \overline{u_\parallel}) \approx \overline{S(P, T, \chi_\alpha, u_\parallel)}, \tag{8}$$

where the overbar denotes the time-averaging operation.

Figure 4 shows an example comparison between the experimental PLIF and CFI on several cross stream planes downstream of the strut injector. Additional comparisons and further details and discussion of the experiments can be found in Drozda et al.[6–8] The PLIF shown in Fig. 4 was obtained using the ${}^{\mathrm{O}}\mathrm{P}_{12}(6.5)$ NO transition line located near 226.9825 nm. The LIF model has been previously shown to perform well for the current flow conditions.[8] The differences observed between the PLIF and CFI are due to flow unsteadiness, geometric differences between adjacent injectors, differences in the fueling levels from different injectors, facility air flow distortion, facility vibration, quality of the experimental optics (including facility windows), laser detuning, laser light absorption (dark bands in the lower portion of the PLIF images), experimental image postprocessing, and finally errors due to turbulence modeling in the CFD. It is difficult to isolate the dominant source of the discrepancies, nevertheless images in Fig. 4 establish a reasonable qualitative level of agreement between the experiments and CFD.

V. Numerical Considerations

The numerical simulations were performed using the Viscous Upwind aLgorithm for Complex flow ANalysis (VULCAN-CFD) code.[19] VULCAN-CFD is a multiblock, cell-centered, finite-volume solver widely used for high-speed flow simulations. For this work, Reynolds-averaged simulations (RAS) were performed. The advective terms were computed using the Monotone Upstream-Centered Scheme for Conservation Laws (MUSCL) scheme[20] with the Low-Dissipation Flux-Split Scheme (LDFSS) of Edwards.[21] The thermodynamic properties of the mixture components were computed using the curve fits of McBride et al.[22] The governing equations were integrated using an implicit diagonalized approximate factorization (DAF) method.[23] All of the turbulence models used in the current work are representative of those used in practical applications. These are: Menter-BSL and -SST,[24] Wilcox-1998 and -2006,[25] and the explicit algebraic Reynolds-stress model (EARSM) of Rumsey and Gatski.[26] Among those, the Menter-BSL model is most commonly used in practice. The models and their common implementations are described in detail on the NASA Langley Research Center Turbulence Modeling Resource website.[27] Additional simulations were also performed using the Wilcox-1998 and -2006 models without the round-jet/planar-jet anomaly corrections[28] typically included with these models. Some simulations also included the realizability corrections of Thivet.[29]

The Reynolds heat flux and species mass flux were modeled using a gradient diffusion model with turbulent Prandtl number ($\mathrm{Pr_t}$) and $\mathrm{Sc_t}$ of 0.9 and 0.5, respectively. To assess the sensitivity of the mixing flowfield to the latter, this value was halved to 0.25 and doubled to 1.0 for some of the simulations. Wilcox wall matching functions[28] were also used, however, their implementation in VULCAN-CFD includes a modification that allows the simulations to recover the integrate-to-the-wall behavior as the value of normalized wall-distance, y^+, approaches one. All simulations were converged until the total integrated mass flow rate and the total integrated heat flux on the walls remained constant to at least 4 decimal points. This typically occurred when the value of the L_2-norm of the steady-state equation-set residual decreased by about 4–5 orders of magnitude.

To conserve the available computational resources, all the simulations were split into elliptic and space-marching (parabolic) regions. The elliptic region contained the inflow of the domain, the injector bodies, and extended up to 6.5 inches downstream of the injection plane. The computational cell count was about equal in both regions, but the computational cost associated with solving the space-marching regions was about an order of magnitude lower than that for the elliptic region. A single, fully elliptic simulation on a coarse grid confirmed that this approach indeed did not have a significant impact on any of the flow features nor the integrated values of the metrics of interest discussed in the previous section.

Three grids, coarse, medium, and fine, each progressively finer by a factor of 2 in each of the three dimensions, were used. The grid resolutions are summarized for the three injector types in Table 2. To reduce the grid size and computational costs, all grids were constructed taking advantage of all available symmetries. That is, only half of the strut, ramp, and flushwall injectors were included in their respective computational domains.

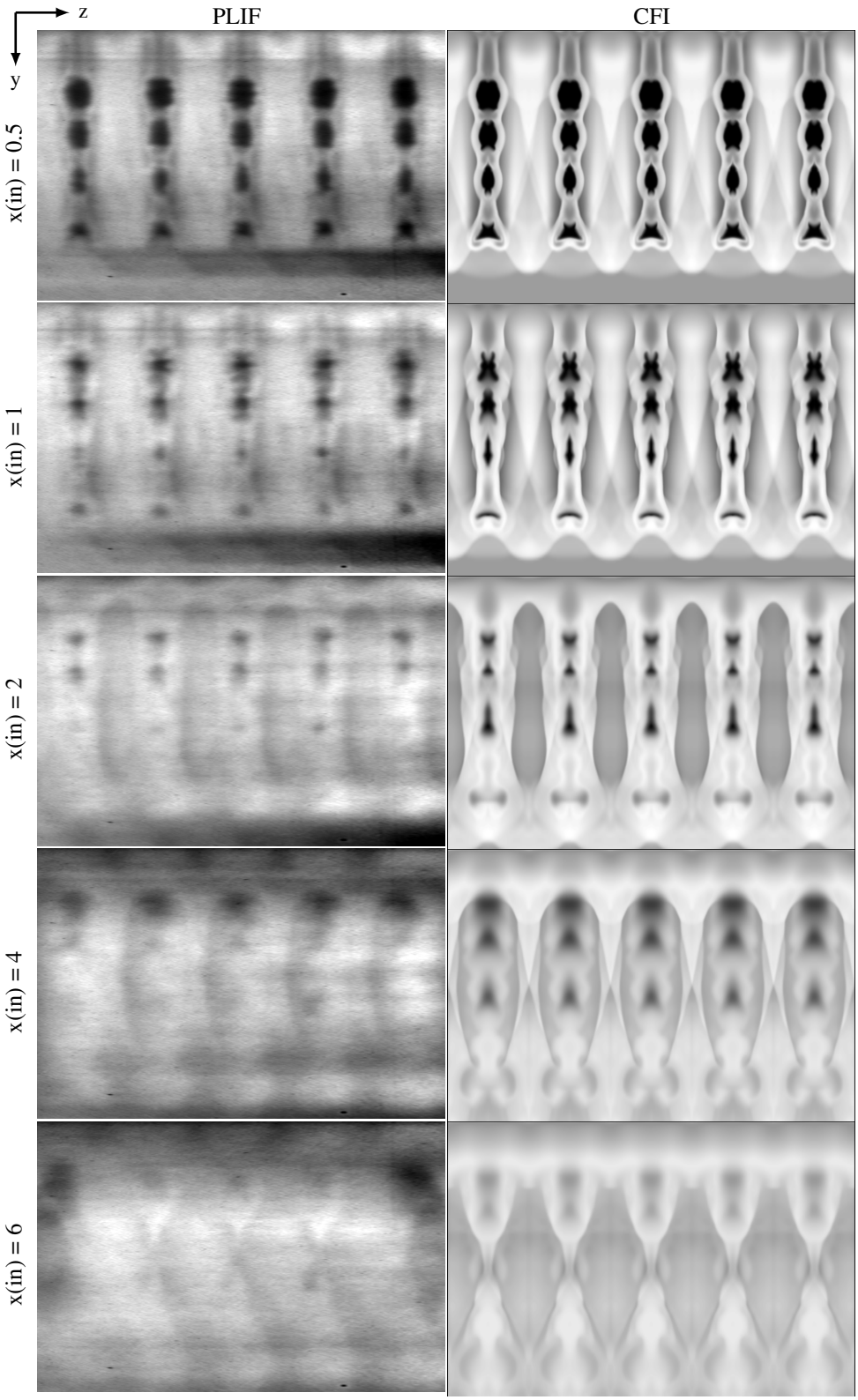

Figure 4. Experimental PLIF and CFIs on several cross stream planes downstream of the strut injector.

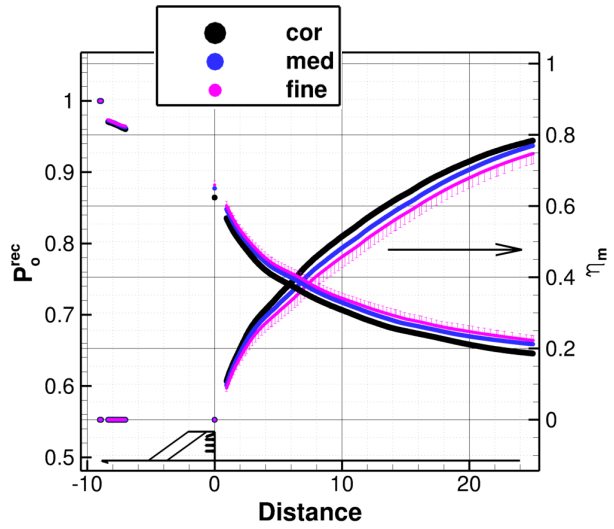

Figure 5. One-dimensional values of the total pressure recovery and mixing efficiency vs. downstream distance (in inches) obtained from the simulations on the coarse, medium, and fine grids, for the strut injector.

All grids were generated with GridPro[30] in the vicinity of the injector bodies and the leading edge of the flat plate, and further combined with Pointwise[31]-generated h-blocks to complete the computational definition of the geometry. For all injectors, the inflow and outflow planes are placed 9 inches upstream and 25 inches downstream of the fuel injection plane, which is located at x = 0. Since both the inflow and the outflow consist of supersonic flow, the mixture composition, static values of the temperature and pressure, and the Mach number are specified at the inflow, and all flow variables are extrapolated at the outflow. Slip wall boundary conditions are used for the upper boundary of the open flat plate flow domain. This upper boundary is 6 inches away from the flat plate, which approximates the height of the facility nozzle core flow. Because the simulation domain effectively includes an infinite row of injectors in the cross-stream, the current simulations model the experiment as an infinitely wide duct. In this modeled 6 inch duct, the flow blockage due to injector bodies in the open plate configuration is 7% and 6.25% for the strut and ramp injectors, respectively. With the exception of the fuel ports, the grid was clustered toward all of the walls with the growth rates varying from 5%–15%. The values of y^+ for these cases, obtained on a fine mesh, were no greater than 20, with the largest values observed on the injector bodies and fuel port walls. The y^+ values along the flat plate are all less than one. The values of y^+ are about two and four times larger for the medium and coarse meshes, respectively.

The line plot of the one-dimensional values of the total pressure recovery and the mixing efficiency versus the downstream distance in inches obtained from the simulations on the coarse (cor), medium (med), and fine grids for the strut injector using the Menter BSL turbulence model and the nominal value of the Sc_t of 0.5 are shown in Fig. 5. Similar results were obtained for the ramp and flushwall injectors. Due to the limitation of the one-dimensional post-processor to analyze only axial planes of data, the plots contain gaps where the complicated grid topology contained streamwise grid "wraps". These "wraps" could have been interpolated onto a Cartesian mesh, however, numerical interpolation of cell center quantities could have introduced additional errors that would be external to the solver. To avoid this, the "wrap" regions were omitted from the grid sensitivity one-dimensional analysis, but are included in the injector performance one-dimensional analysis presented in the results section. The one-dimensional values of the total pressure recovery and the mixing efficiency change monotonically with increasing grid resolution. The error bars

Table 2. Number of computational nodes used in the current simulations.

	Strut	Ramp	Flushwall
Coarse	4,921,682	4,057,382	4,356,936
Medium	39,373,456	32,459,056	34,855,488
Fine	314,987,648	259,672,448	278,843,904

on the fine mesh were obtained assuming a first order accuracy and using the Grid Convergence Index (GCI),[32] which is based on Richardson extrapolation. The resulting error bars are proportional to the difference between the results obtained on the fine and medium meshes, and represent an estimate of the error bounds between the current result and its fully grid-converged value. Although the formal order of accuracy of VULCAN-CFD is second order, first-order accuracy was used for the GCI to ensure a conservative estimate of the errors. Furthermore, visual inspection of the differences between the one-dimensional values of the mixing efficiency, obtained from the simulations on the three different grids, reveals that these data appear to be converging slower than the formal order of accuracy of the solver. It should be noted that this result is not a reflection of the formal order of accuracy of the VULCAN-CFD solver, but rather the impact of shocks on the flow field. To ensure smoothness of the solution near the flow discontinuities and improve the simulation stability, the solver reverts to first-order accuracy near these discontinuities. The observed numerical errors in the total pressure recovery are typically about 0.01–0.02 percent full scale. Typical errors in the computed mixing efficiencies are about 0.02–0.04 percent full scale. Because the differences between the one-dimensional values of the metrics of interest obtained from the simulations on the medium and fine meshes are relatively small, only the results of the simulations obtained on the medium meshes are used in the present work.

VI. Results and Discussion

This section begins by introducing the flow fields for the three baseline injectors used in the study. This is done by examining the contours of the Mach number on the streamwise planes through the centerline of each injector's fuel ports, and on the cross-stream planes both upstream and downstream of the injectors. Line plots of the one-dimensional Mach number, total pressure recovery, and mixing efficiency for three values of the ER are then shown. These simulations are obtained with the Menter-BSL model and $\mathrm{Sc_t}$ of 0.5 and provide a reference for contrast to results obtained for different turbulence models and $\mathrm{Sc_t}$. The sensitivity of the one-dimensional values of the Mach number, total pressure recovery, and the mixing efficiency to turbulence modeling and $\mathrm{Sc_t}$ are shown next. Finally, an assessment of the sensitivity of the CFI is presented in an attempt to ascertain if the experimental PLIF can be extended beyond its intended qualitative visualization purpose and used to guide the turbulence model and $\mathrm{Sc_t}$ selections for the current simulations.

A. Mixing Flow Fields

Mach number contours on the streamwise planes through the centerline of injector ports, and cross-stream planes at various downstream locations obtained from the strut, ramp, and flushwall injector simulations for ER=0.75 and with the Menter-BSL turbulence model and an $\mathrm{Sc_t}$ of 0.5, are shown in Figs. 6, and 7. The images are oriented with the y-axis pointing down for consistency with how the injectors are installed in the EIMP experiments. The flow is left-to-right. The streamwise distance on these figures is in inches. The black isocontour line denotes a helium mass fraction equal to the stoichiometric value for hydrogen (0.0285), which closely approximates the location of the peak heat release in reacting flows and further delineates a boundary of our mixing metric of interest (Eq. (5)). The extent of mixing may be approximately observed by examining the extent of the area enclosed by this isocontour line. The cross-stream planes show the extent to which the mixing plumes spread laterally, which is an indication of the level of potential interaction between the adjacent injectors.

Qualitatively, the flow features for all of the injectors are similar. Upstream, the leading edge of the flat plate causes a shallow bow shock at about 12.5 degrees to the flat plate, which is slightly larger than the Mach wave angle of about 9 degrees for this Mach number. The approach boundary layer thickness is a small fraction of the height of the strut and ramp injector bodies, and the flushwall injector penetration. For the strut and ramp injectors, this results in the injector side body being exposed to the free stream air flow. As a consequence, the boundary layers that develop on the sides of the injector bodies are thin and transitional, which makes them more susceptible to shock-induced separation. Downstream of the injectors, both the streamwise and cross-stream planes show a lower Mach number inside the areas enclosed by the isocontour line, which is characteristic of injection and mixing.

For the strut injector, the downstream mixing plume exhibits a cell-like pattern due to the crossing of shock waves that originate at the leading edge of the strut injector body. As these shock waves pass through the variable density fuel-air interface, vorticity is produced locally due to the effect of the baroclinic torque. The combined action of both the angled injection and the strut injector tip counterrotating vortex pair (CVP) also causes the bifurcation of the mixing plume.

For the ramp injector, an oblique shock wave is generated by the inclined ramp surface of the ramp injector body.

This oblique shock does not interact with the fuel-air mixing plume directly but instead serves primarily to introduce a pressure difference between the top of the ramp surface and the gap between the adjacent injectors. This pressure difference drives the flow to spill from the ramp top surface and introduces CVP around the ramp injector. The size of the vortices is proportional to the ramp height or the gap between injectors, whichever is smaller. When these vortices begin to interact with the injected fuel streams, they stretch and push the fuel-air interface. The combined effect of the angled ramp injection and the vortex entrainment spreads the fuel through the intended fueling area.

For the flushwall injector, the flow features and dynamics are somewhat similar to that of the ramp injector. That is, an oblique bow shock wave is generated by the fuel entering into the supersonic cross-stream. Similar to the shock generated by the ramp body, this oblique shock wave does not interact with the fuel-air mixing. A CVP forms inside the stoichiometric isocontour line. This CVP is driven by the fuel injection process penetrating into the supersonic cross-flow and can be seen at the x = 3 inch station on Fig. 7. The current injection is underexpanded, therefore, some of the dynamic pressure (or momentum) of the fuel jet is "redistributed" in the lateral direction, thereby reducing the amount available for cross-flow penetration. Nevertheless, the penetration is comparable to that of the ramp injector. The primary difference between the flushwall injection and that using a strut or a ramp is that a significant amount of fuel remains in the boundary layer. This effectively reduces the fuel-air interface area (and mixing) as compared to a fully lifted fuel plume.

B. Injector Performance

The Mach number contours obtained from the simulations using various turbulence models and Sc_t are qualitatively comparable and thus omitted for brevity. The effect of turbulence model and Sc_t on the mixing flowfield is most easily assessed using the one-dimensional metrics defined in section III. Figure 8 shows the one-dimensional mass-flux-weighted average Mach number, total pressure recovery, and mixing efficiency computed from simulations using the Menter-BSL model, Sc_t=0.5, and three values of ER: 0.375, 0.75, and 1.5, for the three injectors. These results establish the sensitivity of the one-dimensional quantities to combustor operating conditions as modulated by the ER,

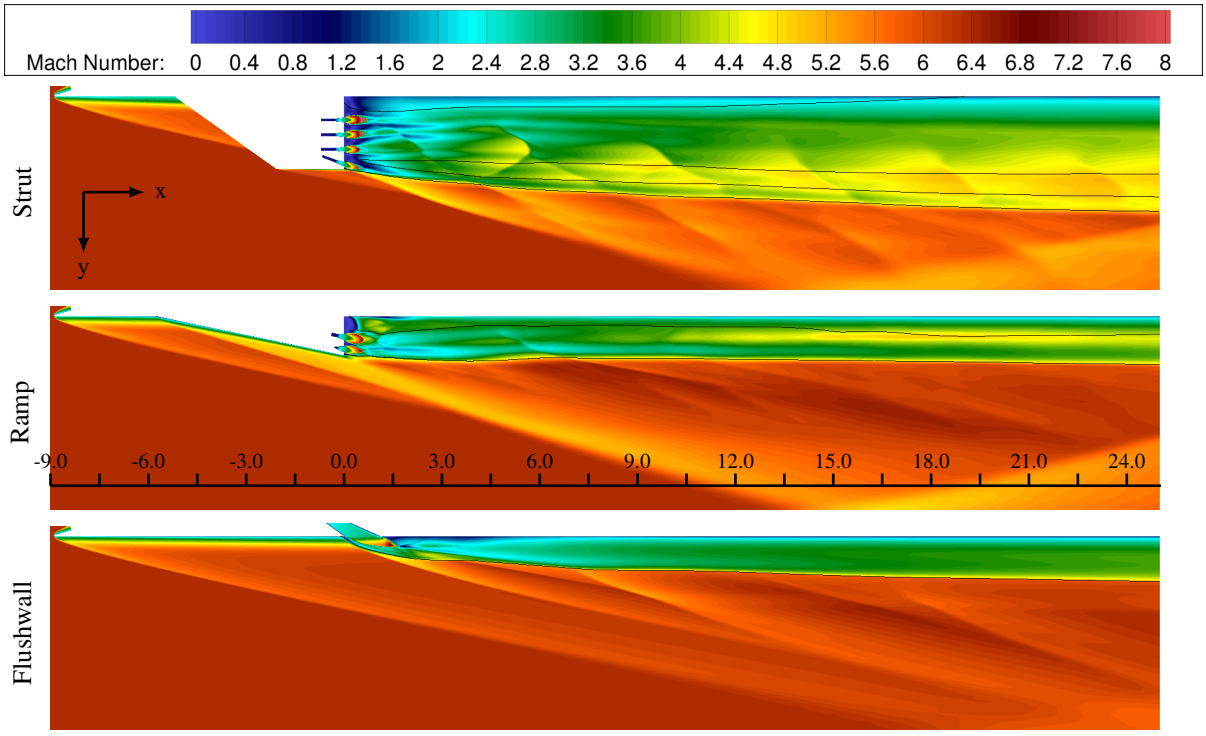

Figure 6. Mach number contours on the streamwise planes through the centerline of injector ports for the strut, ramp, and flushwall injector simulations (distance is in inches). Black isolines denote the helium mass fraction equal to 0.0285.

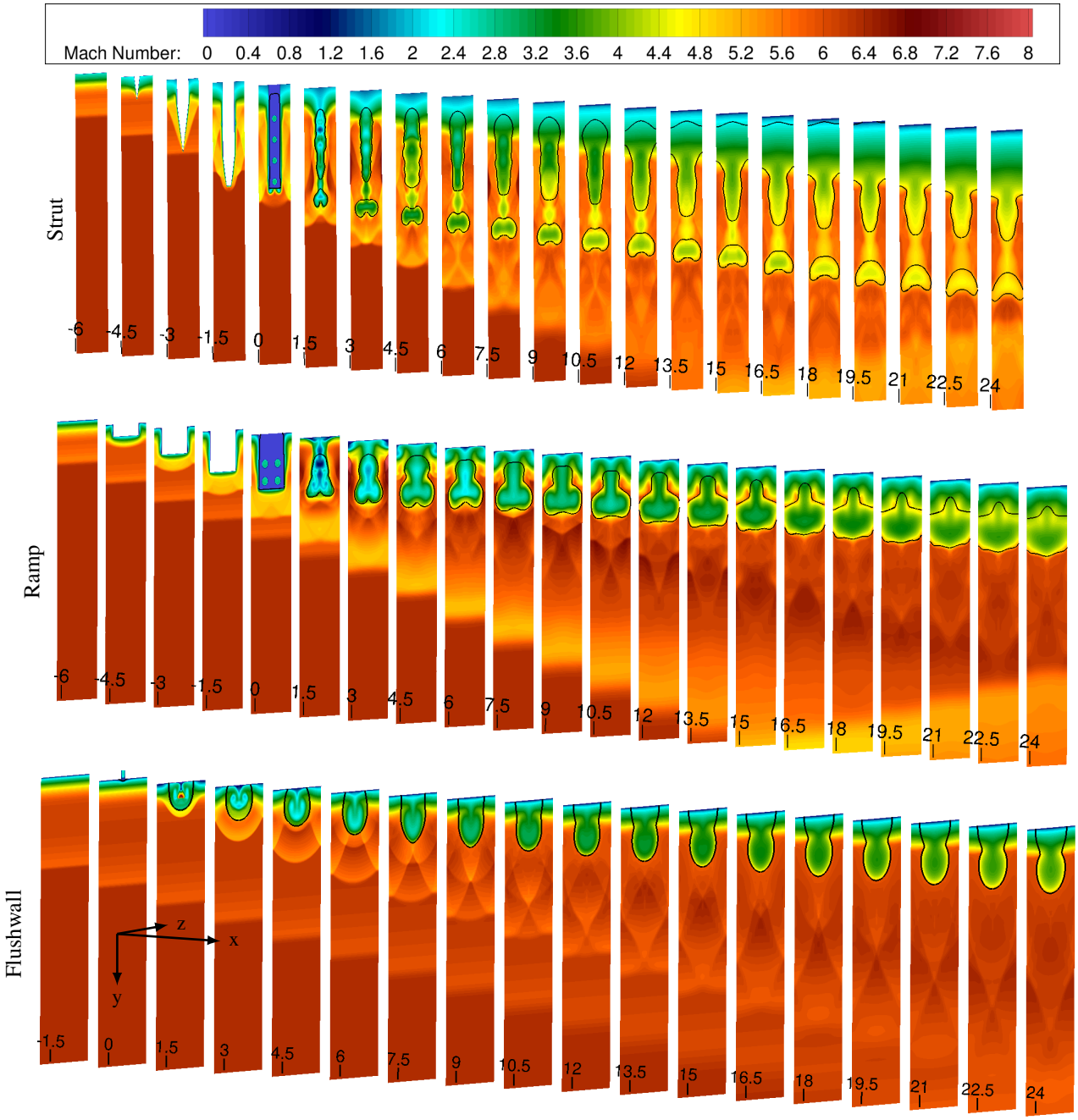

Figure 7. Mach number contours on the cross-stream planes at various downstream locations for the strut, ramp, and flushwall injector simulations (distance is in inches). Black isolines denote the helium mass fraction equal to 0.0285.

and further provide a contrast with the sensitivities due to turbulence modeling discussed next. For a given flight condition, the ER is the primary determinant of the simulation solution space, while, ideally, for a given ER, the turbulence modeling choices should only cause minor departures within that space. As expected, when the ER is low, the losses due to injection and mixing are also the lowest, therefore, the Mach number and the total pressure recovery are the highest. Similarly, the mixing efficiency is also largest because the most air is available for mixing when the ER is low. The converse is true for the largest ER.

The decreases in the values of the one-dimensional Mach number are caused by the effects of the shock waves and friction losses throughout the flowpath and by the mixing losses downstream of the injection plane. The shock waves and drag losses induced by the injectors due to their body geometry are evident by a rapid decrease in the Mach number leading up to the injection plane (i.e., x=0). Downstream of the injection plane, the profiles of the Mach number for the strut and ramp injectors appear to follow a stair-stepping pattern. This effect is caused by the shock waves crossing through, reflecting, and interacting with the mixing plume, and is most pronounced in the strut injector case.

In adiabatic flows, the total pressure recovery can only decrease because it is inversely proportional to the entropy. The decreases are due to shock and viscous losses upstream of the injection plane and also mixing downstream. For the strut and ramp injectors, about 6%–12% of the total pressure losses occur upstream of the injection plane with the strut body inducing almost twice as much loss as the ramp. This is not necessarily surprising because the current strut injector exposes almost twice as much surface area to the flow as the ramp injector, thereby inducing more viscous losses. Furthermore, the included angle of the strut injector is also greater than that of the ramp, resulting in stronger shockwaves.

Downstream of the injection plane, the mixing losses further contribute to the decrease in the total pressure recovery. In general, the losses are proportional to mixing, i.e., greater mixing induces more total pressure loss. Therefore, while the flushwall injector exhibits significantly less mixing than either the strut or the ramp, it also exhibits the

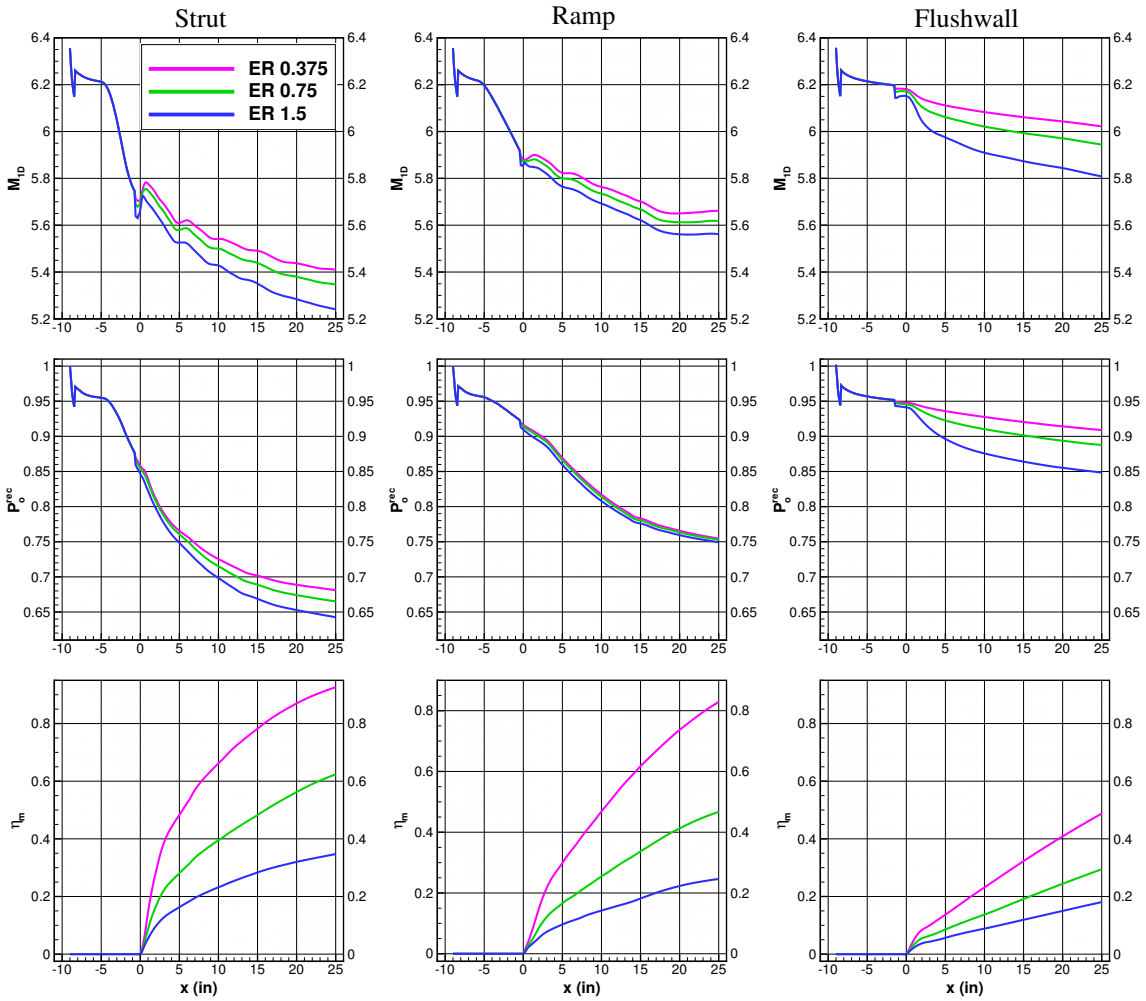

Figure 8. Line plots of the one-dimensional metrics vs. the downstream distance for the strut (left), ramp (middle), and flushwall (right) injector simulations using Menter-BSL, Sc_t=0.5, and different values of the ER.

least amount of total pressure losses. This is a significant observation because the total pressure is proportional to the momentum that can be converted into thrust.

The fuel and air mix the fastest for the strut injector, followed by the ramp, and then the flushwall injectors. This might be expected because, for any ER, the strut injector places each fuel stream inline where it can readily mix with the surrounding air. This fuel placement effect, in addition to the flow blockage and wake introduced by the injector body, results in a rapid rate of mixing in the near field of the strut injection plane. The ramp injector also utilizes an injector body to create blockage and a wake, but the ramp's mixing capabilities are limited by the size and properties of the CVP, which are difficult to design and control across the flight envelope. Nevertheless, although the initial rate of mixing for the ramp injector is reduced as compared to that of the strut, the mixing curve shapes are very similar for both injectors. Compared to the strut and ramp injectors, the flushwall injector exhibits the lowest initial rate of mixing and a fairly linear increase in the mixing efficiency with downstream distance. This is somewhat interesting because, similar to the ramp injector, a strong CVP can be observed forming around and downstream of the flushwall injector (see Fig. 7). However, these vortices primarily act on the fuel rich side of the mixing plume, thereby stirring and inducing losses into the fuel itself rather than at the fuel-air interface, where it could improve mixing. This observation highlights the need for optimization of injection designs in order to fully take advantage of any loss-inducing vortical features that are intentionally introduced into the flowfield.

C. Sensitivity to Turbulence Model and $\mathrm{Sc_t}$

The sensitivity of the one-dimensional values of the mass-flux-weighted average Mach number, total pressure recovery, and mixing efficiency to turbulence modeling choices for the strut, ramp, and flushwall injectors are shown in Figs. 9, 10, and 11, respectively. For plots that compare the simulations utilizing various turbulence models, the nominal $\mathrm{Sc_t}$ and ER are 0.5 and 0.75, respectively. For plots that compare the simulations utilizing various $\mathrm{Sc_t}$, the nominal turbulence model is the Menter-BSL and the ER is 0.75. For the strut injector only, "laminar" simulations (i.e., simulations without any turbulence model) (denoted by No Model), and using Wilcox models without round-jet/planar-jet anomaly corrections[28] (denoted by -NP) were also performed. For the ramp injector, the impact of the realizability corrections of Thivet,[29] instead of the turbulence models, is assessed at the three values of ER. Several observations can be made from the results shown in Figs. 9-11. First, the $\mathrm{Sc_t}$ has a weak influence on both the Mach number and the total pressure recovery. Second, the realizability correction, studied for the ramp simulations, has a weak influence on all one-dimensional metrics. Third, the choice of the turbulence model has a modest influence on the Mach number and total pressure recovery, and significant influence on the mixing efficiency, comparable in magnitude to the effects of varying the ER from 0.375 to 1.5. The influence of the $\mathrm{Sc_t}$ on the mixing efficiency is also significant and similar to that of the turbulence model. As expected, a simulation without a turbulence model produces the least mixing because it lacks the turbulence model contribution to the scalar diffusion. The largest mixing is induced by the EARSM model, which indicates that this model produces the largest values of the eddy viscosity at the fuel-air interface. Even relatively modest corrections to the models, like the round-jet/planar-jet anomaly correction[28] (denoted by -NP) included with the Wilcox models, can reduce the eddy viscosity and impart changes to the mixing efficiency on par with those observed for various $\mathrm{Sc_t}$. It should be noted that all of the models utilized in the present study are routinely used by RAS practitioners in the field, which underscores the requirement for robust experimental data, high-fidelity simulations (e.g., DNS, LES), or extensive subject matter expertise to help narrow down the modeling choices for RAS. It should be further noted, that for the current simulations, the predictions that use the Menter-BSL and Menter-SST models lie about midway of the group. This does not mean that these results are in any way more correct than others, however, when combined with a reasonable range (i.e., 0.1-1.5) of values for the $\mathrm{Sc_t}$, Menter models would offer a practitioner a greater access to the solution space when calibrating with the experimental data.

D. Flow Visualizations for Turbulence Model Selection

For problems of engineering interest, high-fidelity (i.e., scale-resolving) simulations are impractical. In addition, in high-speed flow applications, the experimental data is usually limited to wall measurements (i.e., pressure, temperature, heat flux). One-dimensional metrics, such as those considered above, are generally not available experimentally because they require simultaneous in-stream measurements of a number of thermodynamic quantities and mass flux distribution. However, in the EIMP experiments, nonintrusive flow visualizations using NO-PLIF are obtained. These visualizations represent a nonlinear combination of a number of thermodynamic variables, as shown in Eq. 6, and were previously used to successfully identify several "global" issues with the RAS simulations, such as incorrect wall

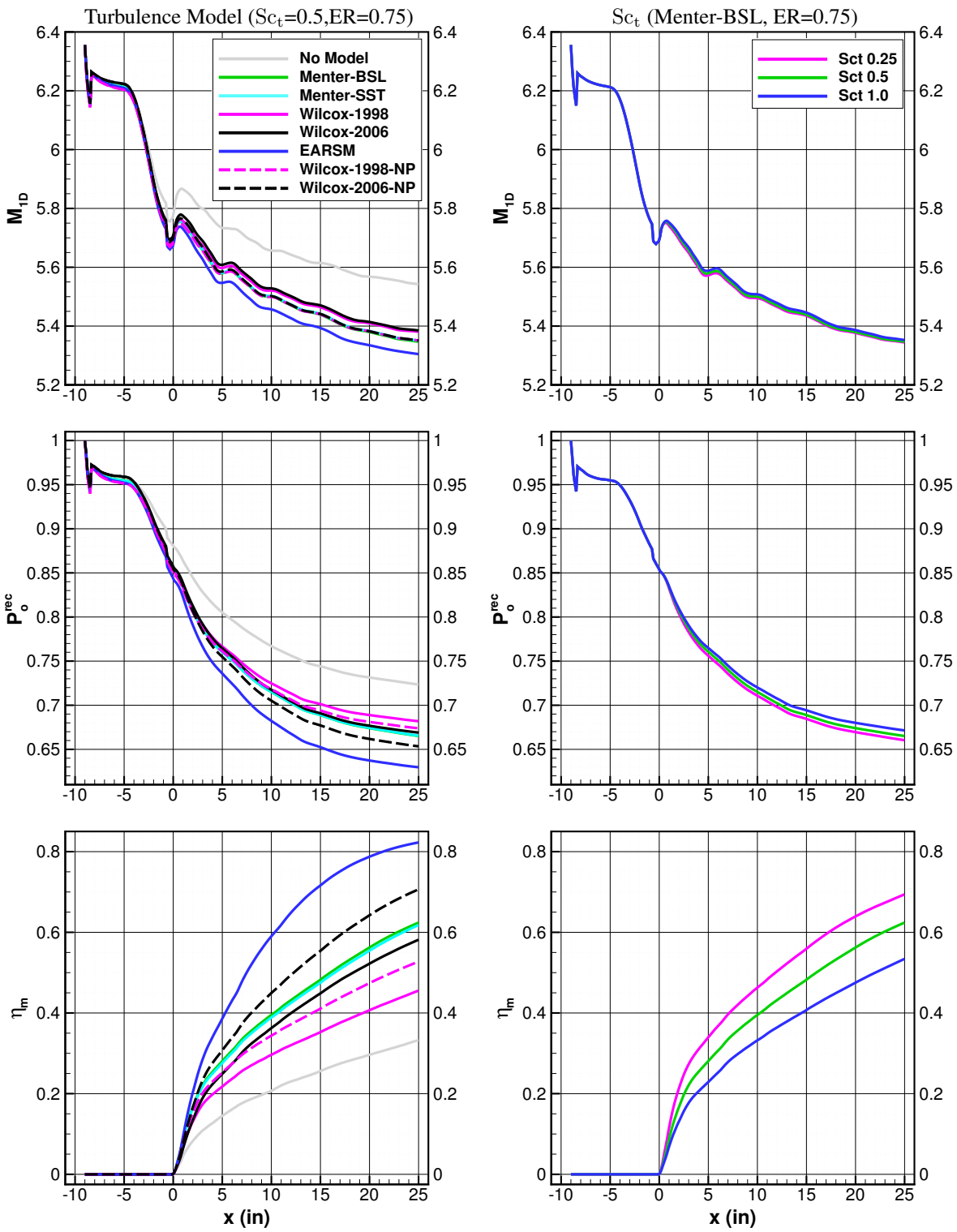

Figure 9. Line plots of the one-dimensional metrics vs. the downstream distance for the strut injector simulations with various turbulence models (left column) and $\mathrm{Sc_t}$ (right column).

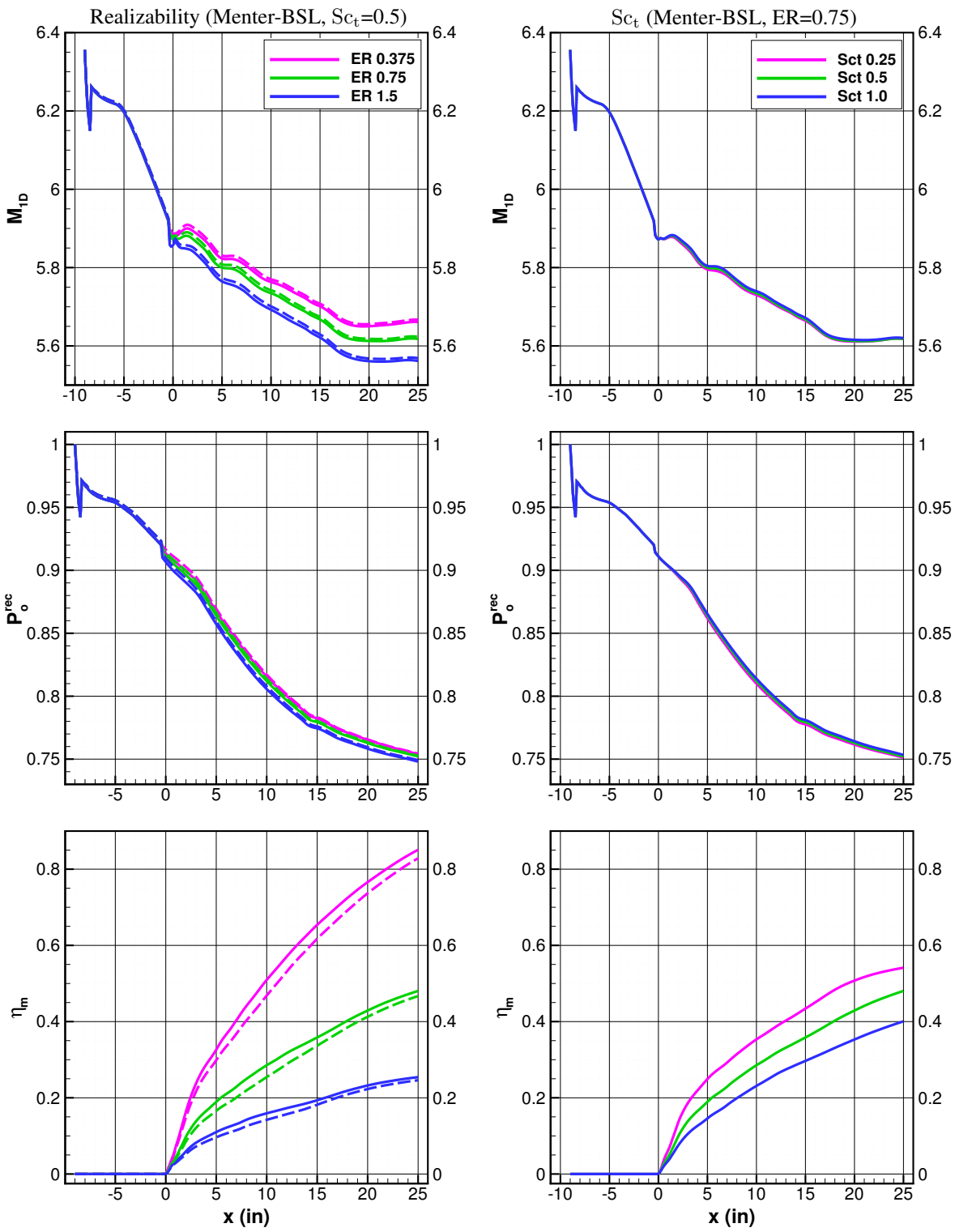

Figure 10. Line plots of the one-dimensional metrics vs. the downstream distance for the ramp injector simulations with (solid) and without (dashed) turbulence model realizability constraints (left column), and with different $\mathrm{Sc_t}$ (right column).

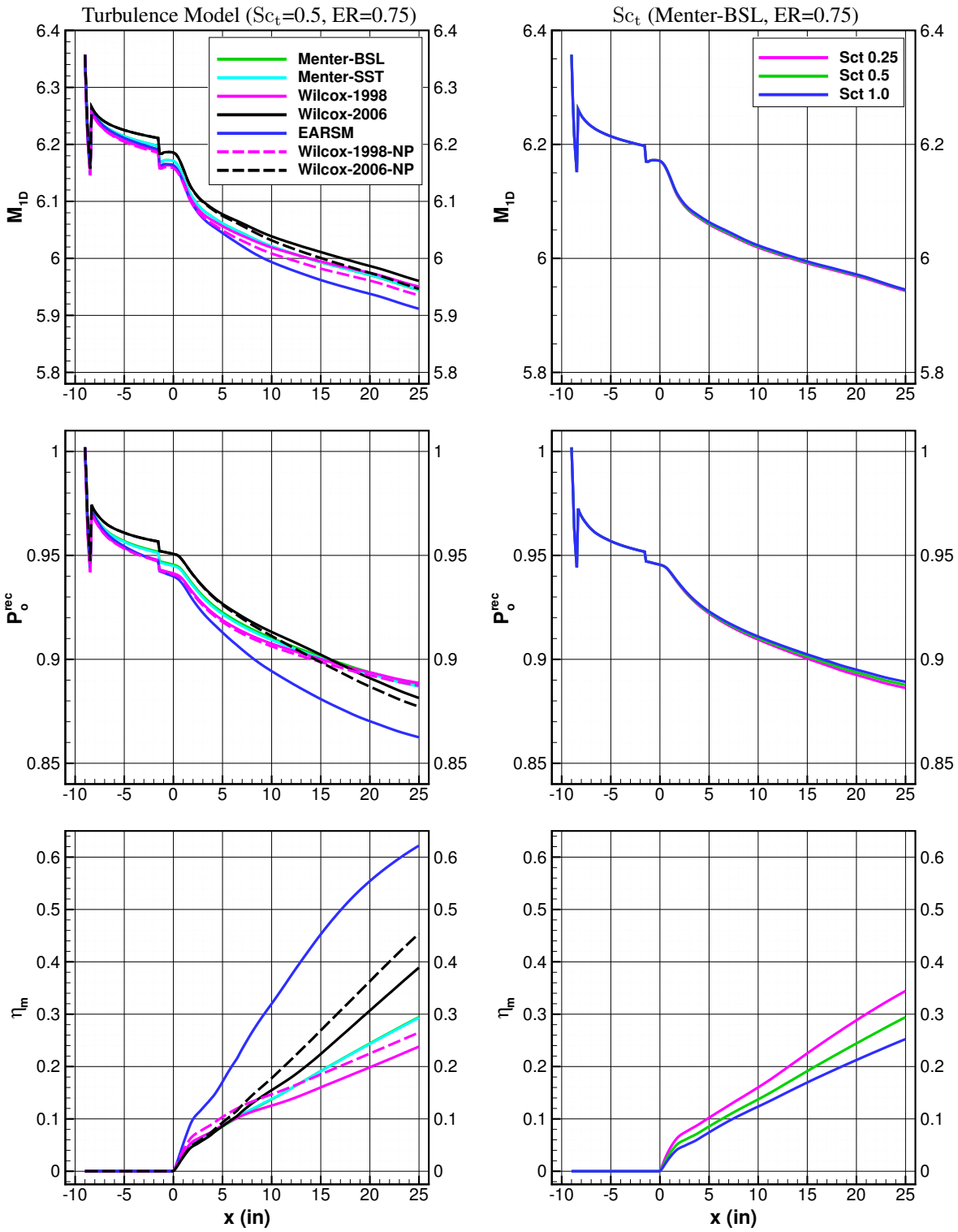

Figure 11. Line plots of the one-dimensional metrics vs. the downstream distance for the flushwall injector simulations with different turbulence models (left column) and Sc_t (right column).

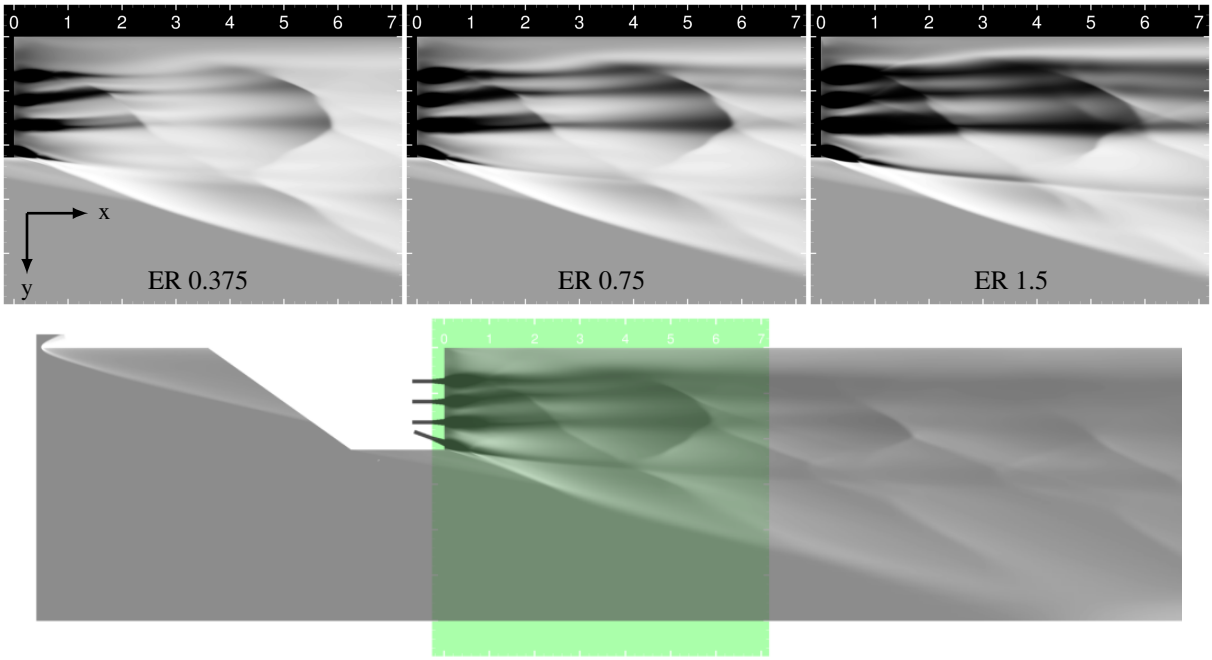

Figure 12. CFIs on the plane through the injector centerline for the strut injector simulations using different ERs. The green area on the lower large image denotes the focus of the smaller images. (dimensions are in inches)

temperature boundary conditions and the early onset of turbulent flow transition which made the strut-body boundary layers less susceptible to flow separation, as discussed by Drozda et al.[7]

Figure 12 shows the CFIs obtained from the simulations using the Menter-BSL model with $\mathrm{Sc_t}$=0.5 and with three different values of the ER for the strut injector. The green area in this figure highlights the focus of the current and all subsequent CFIs, which show the intensity of the LIF signal normalized between zero (black) and one (white) on an xy-plane through the center of the strut injector. As a reminder, because NO is present in the facility air and no NO is seeded into the fuel, the fuel plumes appear dark and can only fluoresce after mixing with the facility air which contains the NO. It should also be noted these synthetic visualizations are presented as a point of reference for further assessment of their sensitivity to the turbulence models and $\mathrm{Sc_t}$. Although specific values of image intensity can be plotted along lines of constant x, it is beneficial to first visually examine the extent to which these images differ. The most notable difference is the increasing persistence of dark fuel bands as the ER increases. This is expected because, as discussed previously, the mixing efficiency decreases as the ER increases. Therefore, there exists less NO-containing air in the fuel stream for higher values of ER, hence less fluorescence and larger regions with low signal intensity. The other features in these images, mainly the shocks, remain comparable between the CFIs.

Figures 13 and 14 show the CFIs obtained from the CFD simulations with ER=0.75 and using various turbulence models for $\mathrm{Sc_t}$=0.5, and various $\mathrm{Sc_t}$ for Menter-BSL turbulence model, respectively. Given the fact that neither the turbulence model nor the $\mathrm{Sc_t}$ significantly impact the inviscid flow structures of this flowfield, not surprisingly, the differences between these images are localized around the fuel plumes. The visual differences are consistent with the one-dimensional values of the mixing efficiency shown in Fig. 9. That is, when the mixing efficiency is lower, e.g., Wilcox-1998 or $\mathrm{Sc_t}$ of 1, then the fuel plumes remain darker further downstream indicating less PLIF signal and therefore, more unmixed fuel. The opposite is also true. That is, when the mixing is more rapid, e.g., EARSM or $\mathrm{Sc_t}$ of 0.25, then the NO in the facility air mixes more rapidly with the helium gas thereby enabling the fuel plumes to fluoresce and appear less dark downstream of the injection plane.

The main features in these images are similar to those discussed for the ER simulations. Despite a fairly large mixing efficiency range (see Fig. 9), the CFIs of the fuel plumes for the simulations utilizing different turbulence models are visually quite similar to one another. In particular, the differences between Menter-BSL and Menter-SST, and Wilcox-1998 and Wilcox-2006 are nearly imperceptible. These observations suggest that it would be difficult

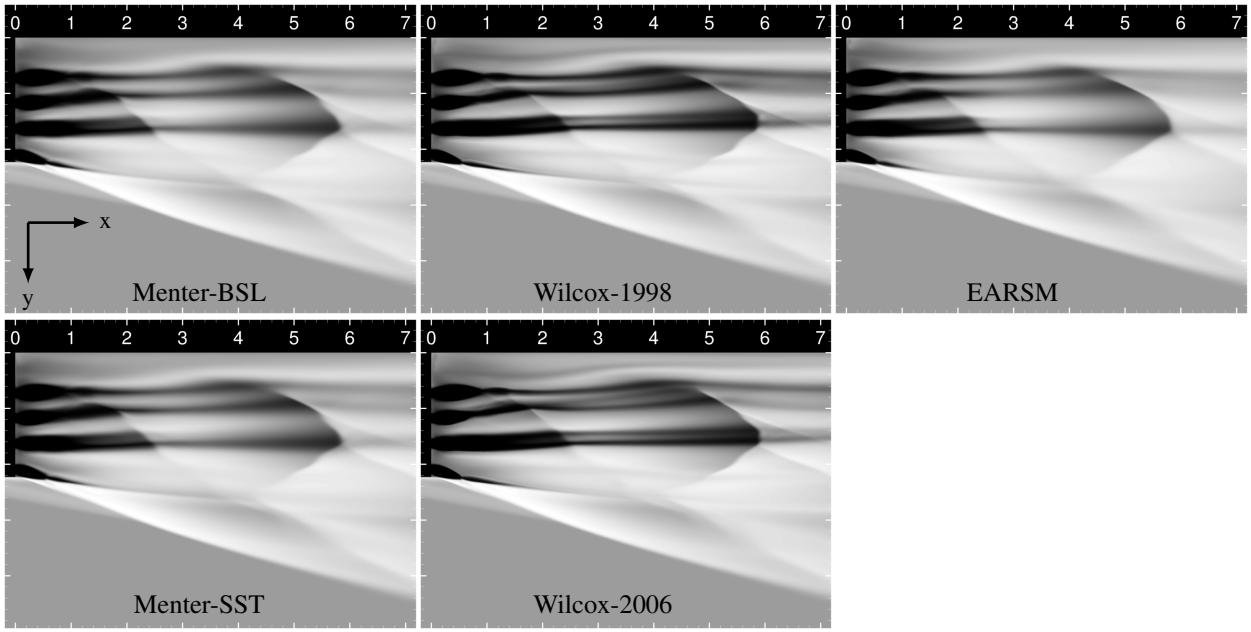

Figure 13. CFIs on the plane through the injector centerline for the strut injector simulations using different turbulence models for $\mathrm{Sc_t}$=0.5. The focus area is the same as in Fig. 12. (dimensions are in inches)

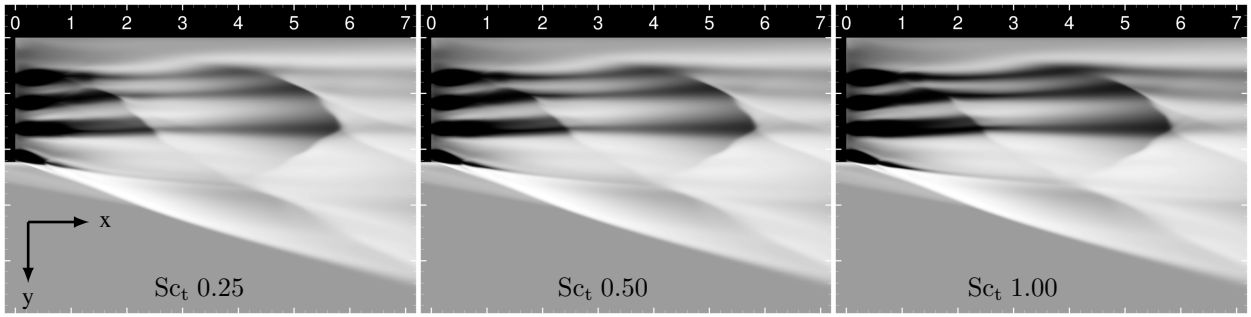

Figure 14. CFIs on the plane through the injector centerline for the strut injector simulations using different $\mathrm{Sc_t}$ and Menter-BSL turbulence model. The focus area is the same as in Fig. 12. (dimensions are in inches)

to utilize PLIF visualizations to guide the turbulence model selection for the CFD. However, for a given turbulence model, it may be possible to use CFI to narrow down the value of the $\mathrm{Sc_t}$ because the differences between the CFI images corresponding to various $\mathrm{Sc_t}$ are a bit more pronounced.

To determine whether the differences in the CFI image intensities observed for various $\mathrm{Sc_t}$ are sufficiently large to use for selecting its value from PLIF visualizations, several lines at 1, 2, 4, and 6 inches downstream from the strut injector are extracted from the CFI images obtained using the Menter-BSL turbulence model for the ER of 0.75, and plotted vs. the vertical distance from the plate. Data at 0.5 inches downstream of the injector were not used because it exhibits almost no sensitivity to the $\mathrm{Sc_t}$ due to limited mixing at this near-field location. Fig. 15 shows these lines for the various $\mathrm{Sc_t}$. Experimental data points, extracted at the same locations from the PLIF images of Fig. 4 are denoted by black symbols. Because the experimental PLIF images include five injector centerlines, rather than plotting only a center-most injector centerline, the three central injector centerlines are plotted. The end injectors are excluded to limit the impact of the edge effects on the experimental data. Because PLIF images are time averaged, plotting

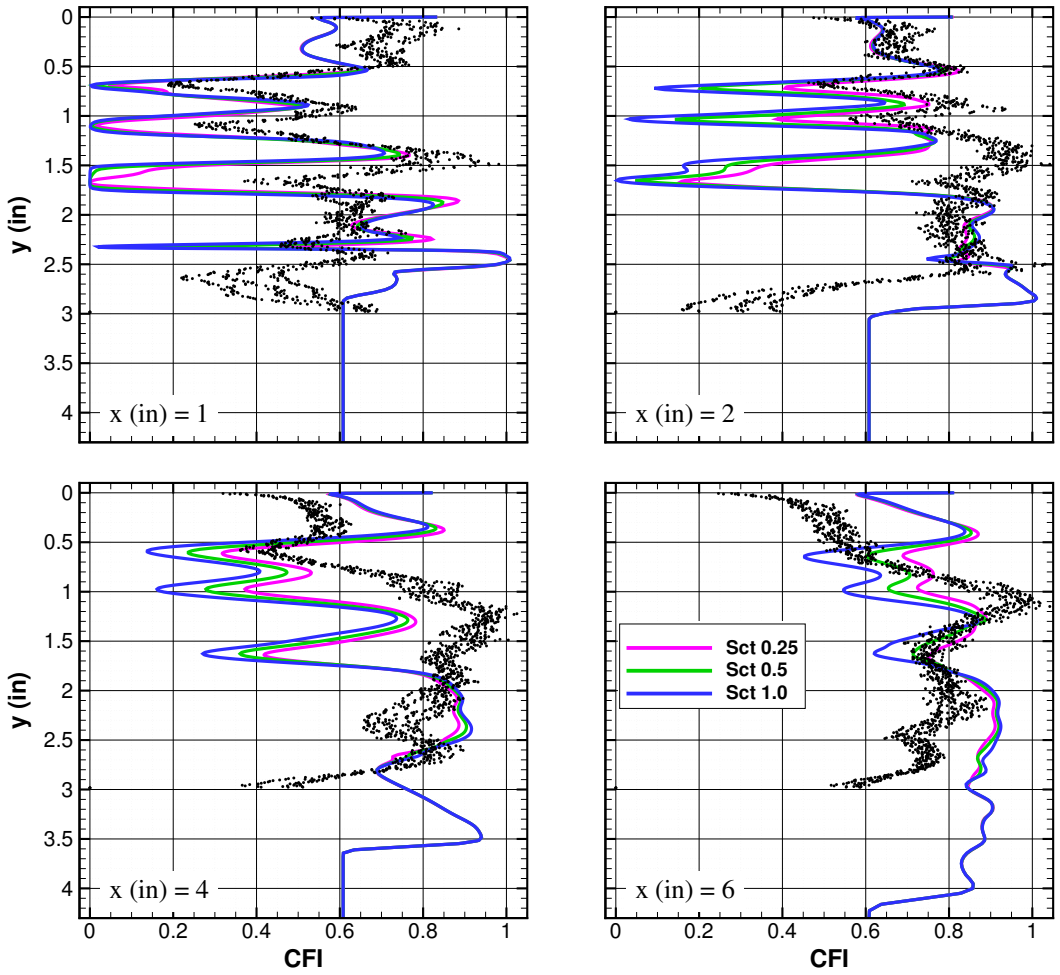

Figure 15. Line plots of the vertical distance from the plate in inches vs. LIF signal extracted from the CFIs at the centerline and various downstream locations for the strut injector simulations using different $\mathrm{Sc_t}$. The experimental data is denoted by the symbols.

multiple injector centerlines from a single PLIF image provides an estimate of the minimum amount of experimental and postprocessing uncertainty in the PLIF. The total uncertainty is much larger and a combination of various factors that include geometric differences between adjacent injectors, differences in the fueling levels from different injectors, facility air flow distortion, facility vibration, quality of the experimental optics (including facility windows), laser detuning, laser light absorption, and experimental image postprocessing. Nevertheless, although the general trends between the CFI and PLIF are comparable, especially in the near field, the range of the data scatter due to experimental uncertainties is similar to the differences in the image intensities due to the variable $\mathrm{Sc_t}$. Therefore, without further reducing the experimental uncertainties, PLIF visualization could likely be used only in a very limited manner to guide the selection of the $\mathrm{Sc_t}$. For example, current PLIF suggests a higher level of mixing than the simulations, therefore, values of the $\mathrm{Sc_t}$ of less than 0.5 might be appropriate. This observation is consistent with the fact that, similar to hydrogen, helium has a smaller value of the molecular Schmidt number (Sc), and therefore diffuses faster than other gases in air.

VII. Summary and Conclusions

A CFD study was conducted to investigate the sensitivity of the mixing characteristics and calculated performance of three types of fuel injectors at hypervelocity flow conditions to turbulence modeling choices. The injectors consist of a strut, ramp, and flushwall injector. These injectors represent three main categories of injectors typically considered individually or in combination for fueling the propulsive devices used for high-speed flight. The turbulence modeling choices included five turbulence models typically used in practical applications, and the turbulent Schmidt number. The latter is a key modeling parameter in simulations of turbulent mixing and reacting flows. Results of the Reynolds-Averaged Simulations (RAS) revealed that the inviscid flow features are weakly impacted by the turbulence modeling choices as illustrated by the relatively small changes of the one-dimensional values of the mass-flux-weighted average Mach number. However, the one-dimensional values of the mixing efficiencies showed a significant sensitivity with respect to both the choice of the turbulence model and the turbulent Schmidt number. This result is well known and is the main driver behind advancing higher-fidelity CFD simulations for applications to mixing and reacting flows. The turbulent Schmidt number is also the main parameter used for calibrating mixing and reacting RAS to the experimentally available data. In addition, a numerical assessment is made of the sensitivity of the CFI (i.e., synthetic PLIF) to the turbulence modeling choices. This was accomplished by modeling and computing the synthetic PLIF signal from the CFD data for various turbulence models and turbulent Schmidt numbers and generating computational flow images (CFIs) equivalent to PLIF. This assessment was made to investigate the possibility of calibrating the RAS using experimentally-obtained PLIF visualization data. CFIs obtained from the RAS using various turbulence models and turbulent Schmidt numbers showed that LIF is not highly sensitive to the modeling choices. The differences between the CFIs were subtle and concentrated around the fuel plumes. Furthermore, comparison between the CFIs and the experimental PLIF data showed that it would be difficult to utilize PLIF to effectively guide both turbulence model and turbulent Schmidt number selections for the CFD. Nevertheless, the analysis provides a quantitative estimate of the needed PLIF signal fidelity to resolve the subtle mixing differences among the different cases and enable RAS model calibration.

Acknowledgments

This work is supported by the Hypersonic Technology Project in the Advanced Air Vehicles Program of the NASA Aeronautics Research Mission Directorate (ARMD). Computational resources are provided by the NASA Langley Research Center and the NASA Advanced Supercomputing (NAS) Division.

References

[1] Lee, J., Lin, K.C., and Eklund, D., "Challenges in Fuel Injection for High-Speed Propulsion Systems," *AIAA J.*, Vol. 53, No. 6, 2015, pp. 1405–1423.

[2] Cabell, K., Drozda, T.G., Axdahl, E.L., and Danehy, P.M., "The Enhanced Injection and Mixing Project at NASA Langley," in *JANNAF 46th CS / 34th APS / 34th EPSS / 28th PSHS Joint Subcommittee Meeting*, NTRS Report Number NF1676L-25526, Albuquerque, NM, 2014.

[3] Cabell, K.F. and Rock, K.E., "A Finite Rate Chemical Analysis of Nitric Oxide Flow Contamination Effects on Scramjet Performance," Tech. Rep. TP-2003-212159, NASA, 2003.

[4] Drozda, T.G., Drummond, J.P., and Baurle, R.A., "CFD Analysis of Mixing Characteristics of Several Fuel Injectors at Hypervelocity Flow Conditions," in *52nd AIAA/SAE/ASEE Joint Propulsion Conference*, AIAA 2016-4764, AIAA, Salt Lake City, UT, 2016.

[5] Drozda, T.G., Baurle, R., and Drummond, J.P., "Impact of Flight Enthalpy, Fuel Simulant, and Chemical Reactions on the Mixing Characteristics of Several Injectors at Hypervelocity Flow Conditions," in *63rd JANNAF Propulsion Meeting / 47th CS / 35th APS / 345h EPSS / 29th PSHS Joint Subcommittee Meeting*, NTRS Report Number NF1676L-23113, Newport News, VA, 2016.

[6] Drozda, T.G., Cabell, K.F., Ziltz, A.R., Hass, N.E., Inman, J.A., Burns, R.A., Bathel, B.F., Danehy, P.M., Abul-Huda, Y.M., and Gamba, M., "Comparisons Between NO PLIF Imaging and CFD Simulations of Mixing Flow-

fields for High-Speed Fuel Injectors," in *53rd AIAA/SAE/ASEE Joint Propulsion Conference, AIAA Propulsion and Energy Forum*, AIAA 2017-4647, AIAA, Atlanta, GA, 2017.

[7] Drozda, T.G., Cabell, K.F., Ziltz, A.R., Hass, N.E., Inman, J.A., Burns, R.A., Bathel, B.F., and Danehy, P.M., "Comparison Between NO PLIF Imaging and CFD Simulations of Mixing Flowfields for High-Speed Fuel Injectors," in *JANNAF Meeting / 48th CS / 36th APS / 36th EPSS / 30th PSHS Joint Subcommittee Meeting*, NTRS Report Number NF1676L-27198, Newport News, VA, 2017.

[8] Drozda, T.G., Ground, C.R., Ziltz, A.R., Cabell, K.F., Inman, J.A., Bathel, B.F., and Danehy, P.M., "Analysis of the Two-Level NO PLIF Model for Low-Temperature High-Speed Flow Applications," in *AIAA International Space Planes and Hypersonic Systems and Technologies Conference*, Orlando, FL, 2018.

[9] Baurle, R.A., Fuller, R.P., White, J.A., Chen, T.H., Gruber, M.R., and Nejad, A.S., "An Investigation of Advanced Fuel Injection Schemes for Scramjet Combustion," in *36th Aerospace Sciences Meeting and Exhibit*, Reno, NV, 1998.

[10] Ogawa, H., "Physical Insight into Fuel-Air Mixing for Upstream-Fuel-Injected Scramjets via Multi-Objective Design Optimization," *J. Propul. Power.*, Vol. 31, No. 6, 2015, pp. 1505–1523.

[11] Brown, G.L. and Roshko, A., "On Density Effects and Large Structure in Turbulent Mixing Layers," *J. Fluid Mech.*, Vol. 64, 1974, pp. 775–816.

[12] Bogdanoff, D.W., "Compressibility Effects in Turbulent Shear Layers," *AIAA J.*, Vol. 21, No. 6, 1983, pp. 926–927.

[13] Papamoschou, D. and Roshko, A., "The Compressible Turbulent Shear Layer: An Experimental Study," *J. Fluid Mech.*, Vol. 197, 1988, pp. 453–477.

[14] Riggins, D.W., McClinton, C.R., and Vitt, P.H., "Thrust Losses in Hypersonic Engines Part 1: Methodology," *J. Propul. Power.*, Vol. 13, No. 2, 1997, pp. 281–287.

[15] Mao, M., Riggins, D.W., and McClinton, C.R., "Numerical Simulation of Transverse Fuel Injection," in *Computational Fluid Dynamics Symposium on Aeropropulsion*, NASA-CP-3078, NASA, Cleveland, OH, 1990, pp. 635–667.

[16] Paul, P.H., Gray, J.A., Durant Jr., J.L., and Thoman Jr., J.W., "A Model for Temperature-Dependent Collisional Quenching of NO $A^2\Sigma^+$," *Appl. Phys. B*, Vol. 57, 1993, pp. 249–259.

[17] Ivey, C.B., Danehy, P.M., Bathel, B.F., Dyakonov, A.A., Inman, J.A., and Jones, S.B., "Comparison of PLIF and CFD Results for the Orion CEV RCS Jets," in *49th AIAA Aerospace Sciences Meeting*, AIAA-2011-713, AIAA, Orlando, FL, 2011.

[18] Luque, J. and Crosley, D.R., "LIFBASE: Database and Spectral Simulation Program (Version 1.5)," Tech. Rep. MP 99-009, SRI International, 1999.

[19] VULCAN-CFD, "http://vulcan-cfd.larc.nasa.gov/," 2017.

[20] van Leer, B., "Towards the Ultimate Conservative Difference Scheme. V: A Second-Order Sequel to Godunov's Method," *J. Comput. Phys.*, Vol. 32, No. 1, 1979, pp. 101–136.

[21] Edwards, J.R., "A Low-Diffusion Flux-Splitting Scheme for Navier-Stokes Calculations," *Comput. Fluids.*, Vol. 26, No. 6, 1997, pp. 635–659.

[22] McBride, B.J., Gordon, S., and Reno, M.A., "Thermodynamic Data for Fifty Reference Elements," NASA Technical Paper 3287/REV1, NASA, Cleveland, OH, 2001.

[23] Pulliam, T.H. and Chaussee, D.S., "A Diagonal Form of an Implicit Approximate-Factorization Algorithm," *J. Comput. Phys.*, Vol. 39, No. 2, 1981, pp. 347–363.

[24] Menter, F.R., "Two-Equation Eddy-Viscosity Turbulence Models for Engineering Applications," *AIAA J.*, Vol. 32, No. 8, 1994, pp. 1598–1605.

[25] Wilcox, D.C., "Formulation of the $k-\omega$ Turbulence Model Revisited," *AIAA J.*, Vol. 46, No. 11, 2008.

[26] Rumsey, C.L. and Gatski, T.B., "Summary of EASM Turbulence Models in CFL3D with Validation Test Cases," NASA/TM 2003-212431, NASA Langley Research Center, Hampton, VA, 2003.

[27] Rumsey, C., "NASA Langley Research Center Turbulence Modeling Resource," https://turbmodels.larc.nasa.gov, 2017.

[28] Wilcox, D.C., *Turbulence Modeling for CFD*, DCW Industries, Inc., La Cañada, CA, 2006.

[29] Thivet, F., Knight, D.D., Zheltovodov, A.A., and Maksimov, A.I., "Insights in Turbulnece Modeling for Crossing-Shock-Wave/Boundary-Layer Interactions," *AIAA J.*, Vol. 39, No. 6, 2001, pp. 985–995.

[30] Program Development Company, "GridPro - Automatic Multiblock Grid Generation Software," http://www.gridpro.com/, 2017.

[31] Pointwise, Inc., "Pointwise: Mesh Generation Software for CFD," http://www.pointwise.com/, 2017.

[32] Roache, P.J., *Verification and Validation in Computational Science and Engineering*, Hermosa Publishers, 1998.